International Journal of Fatigue 172 (2023) 107664

Contents lists available at ScienceDirect

International Journal of Fatigue

journal homepage: www.elsevier.com/locate/ijfatigue

Selective laser melted 316L stainless steel: Influence of surface and inner defects on fatigue behavior

Barbara Rivolta, Riccardo Gerosa *, Davide Panzeri

Department of Mechanical Engineering, Politecnico di Milano, Italy

ARTICLE INFO

Keywords:
Stainless steel
Fatigue limit
Defects
S-N curves
Fractography

ABSTRACT

In additive manufacturing, despite its several indisputable advantages, detrimental variables to fatigue strength still remain poor surface finishing and porosities. However, because the majority of defects locate close to the surface, their mechanical removal is expected to appreciably improve fatigue strength. Considering SLMed 316L, fully-reversed rotating-bending fatigue tests in both as-built and machined conditions are performed. Fatigue failures are discussed using the Kitagawa-Takahashi diagram. In each condition, the fatigue stress is related to the equivalent micro-notch length of the killer defect. Then, this work analyses the possibility of predicting fatigue limits at 50 % probability considering the equivalent micro-notch length.

1. Introduction

In the last decades, additive manufacturing has been exponentially adopted in several industrial fields, such as biomedical, space, automotive and aircraft industries. Service applications can involve a wide variety of complex dynamic loading conditions and a reliable structural integrity becomes really important [1]. This innovative technology provides several benefits in comparison to conventional manufacturing methods because of design flexibility and efficient use of resources. Nevertheless, the forming principles are really different with respect to those of conventional subtractive techniques [1–14].

According to literature, in the as-built condition, SLMed 316L stainless steel is characterized by a very fine microstructure and grains elongated in the build direction [14]. This distinctive feature is associated to the presence of really high cooling rates ranging from 10^3 K/s to 10^8 K/s which determine formation of non-equilibrium phases and refined microstructures [15]. For this reason, mechanical properties of SLMed parts are typically improved in comparison to those of conventionally-manufactured castings. This unique property in SLMed materials allows superior tensile properties [3–8,10,13,15,16]. However, presence of internal porosities can dramatically reduce mechanical and fatigue performances which should have been excellent in the absence of such detrimental defects [13,17,18]. Defects formation strongly depends on process parameters whose definition definitely impacts on fatigue performance of additively-manufactured components worsening reliability in high-demanding applications [3,5,13]. For this reason, fatigue properties of additively-manufactured parts are typically poorer in comparison to wrought counterparts [7,13,14,19–23].The main key aspects affecting fatigue properties are surface roughness, intrinsic defects, microstructure and residual stresses [1].

As reported in literature, SLM technique involves a large variety of defects associated to lack of fusion, un-melted particles and gas porosities [1]. Formation of cracks can be also promoted by residual stresses accumulated during the manufacturing process [1,24]. Such defects act as stress concentrators promoting fatigue cracks nucleation with detrimental consequences on fatigue life. Moreover, such defects can enhance localized corrosion attack deteriorating components quality and further stimulating fatigue failure [1]. A summary of the main defect types observed in additively-manufactured components is reported in Table 1. Gas porosities, mainly originated by the trapped gas in the powder and the gas atmosphere, almost always show spherical or ellipsoidal shapes [1]. Formation of gas bubbles in the melt pool can be also determined by excessive energy which induces intense convection currents and vaporization responsible for ejected spatter and instability [1]. On the other hand, when the energy supplied to the melt pool is insufficient, lack of bonding between layers can be obtained with formation of Lack-of-Fusion (LoF) defects almost always characterized by sharp edges [1]. Normally, they contain un-melted or partially melted powder particles. Because of the detrimental influence on fatigue strength, surface and inner defects require a complete characterization in terms of size, morphology, position and distribution [1,25]. Moreover, they are generally not uniformly distributed throughout the printed volume. In fact, defects concentration is higher close to the

* Corresponding author.
E-mail addresses: barbara.rivolta@polimi.it (B. Rivolta), riccardo.gerosa@polimi.it (R. Gerosa), davide.panzeri@polimi.it (D. Panzeri).

https://doi.org/10.1016/j.ijfatigue.2023.107664
Received 17 January 2023; Received in revised form 3 March 2023; Accepted 30 March 2023
Available online 3 April 2023

Nomenclature

Symbols

R	fatigue load ratio
p	defect perimeter
A	defect area
HV	Vickers Hardness
$\Delta\sigma$	stress increment
K	Stress Intensity Factor
σ	applied stress
$\sqrt{area}$	defect size parameter (equivalent micro-notch length)
t	defect depth
d	defect size
e	surface distance of the defect
ΔK_{th}	threshold stress-intensity range
$\Delta\sigma_{th}$	threshold fatigue stress range
$\Delta\sigma_f$	fatigue limit
a_0	El-Haddad intrinsic crack
$\Delta K_{th,LC}$	threshold ΔK for long cracks
$\Delta K_{th,eff}$	intrinsic (effective) ΔK threshold
E	elastic modulus
$\boldsymbol{b}$	Burgers vector
h	Burgers vector component
k	Burgers vector component
l	Burgers vector component
α	constant
a	edge length of the unit cell
$a_o^{'}$	modified a_0 parameter
a^*	additional parameter
σ_f	fatigue limit
a	crack length
Δa	crack extension
σ_{f0}	theoretical fatigue limit
N_f	number of cycles at failure
l/w	length-to-width ratio
WR	wrought
b_2	surface coefficient
σ_a	stress amplitude
Y	constant
R_a	surface roughness parameter
R_t	surface roughness parameter
R_z	surface roughness parameter
R_v	surface roughness parameter
R_c	surface roughness parameter

Acronyms

AM	Additive Manufacturing
LPBF	Laser Powder Bed Fusion
FCC	Face-Centered Cubic
UTS	Ultimate Tensile Strength
YS	Yield Strength
HIP	Hot Isostatic Pressing
LOM	Light Optical Microscope
SEM	Scanning Electron Microscope
K-T	Kitagawa-Takahashi
LoF	Lack-of-Fusion
SLM	Selective Laser Melting

Table 1
Summary of the main defect types observed in additively-manufactured components according to [1].

Type	Features	Cause
Lack of Fusion (LoF)	Non-sintered area or delamination; Improper fusion between successive tracks or layers	Insufficient energy
Un-melted powder	Incomplete powder melting	Insufficient energy
Gas porosity	Entrapped gas	Excessive energy
Keyholing	Improper closure of a keyhole	Excessive energy
Small cracks		Residual stresses
Balling phenomenon	Discontinuity in material	Lack of wetting of solid particles
Surface roughness	Partially-melted powder particles	Layer by layer deposition and powder feed stock; supports

surface and it reduces towards the core because of scanning strategy and thermal gradients [1]. For this reason, reduced amount of residual defects and more uniform distributions can be achieved removing the near surface layer by machining operations. Regarding fatigue performance, surface defects are generally more detrimental than internal ones because local stresses are usually higher in such positions. So, post-processing strategies should be aimed at minimizing defects close to the surface. Moreover, the presence of a large fraction of porosity in sub-surface regions can promote interaction between pores and formation of clusters, even if defects are small.

Despite surface roughness is useful to promote bone growth in medical implants, its influence on fatigue performance is really detrimental [1]. Poor surface finishing of as-built components is determined by the repetitive layer-by-layer nature of the process and partially-melted particles attached to the surface [1,7,22,23]. These features typically interact with sub-surface and surface-connected defects. Surface roughness is affected by process parameters, powder size and component geometry [7,23]. Furthermore, the presence of building supports and their subsequent mechanical removal can dramatically deteriorate the surface quality. Almost all the available literature agrees that surface roughness represents the most important parameter affecting fatigue performance of as-built specimens [1,7,22,23]. In accordance with this observation, appreciable improvements in this property were observed after surface machining operations.

According to the previous observations, fatigue performance of additively-manufactured components can be improved by post processing strategies. Post heat treatments can be properly adopted to obtain a uniform microstructure, remove residual stresses and control phases formation that can further improve strength [1,26]. Adoption of shot peening, sand blasting, machining and polishing operations can improve fatigue performance by reducing surface roughness, near-surface defects and, in the case of shot peening and sand blasting, also creating residual compressive stresses [1,7,9,22,24,27]. In addition, defects content can be further reduced using high quality powder and optimizing process parameters [1]. This observation is also well known in Powder Metallurgy technical literature [28–35]. Hot Isostatic Pressing (HIP) is another post-processing technique. However, in this case, thermal exposure can significantly alter microstructure with coarsening and phases formation. In addition, with HIP, surface and surface-connected defects cannot be removed [1,23]. Moreover, conventional machining and polishing operations cannot be applied to complex lattice parts or thin internal features [1,6]. For this reason, other post-processing techniques should be considered, such as electrochemical and vibratory polishing [1,6]. The cost of post processing operations should be carefully quantified because it can exceed even 50 % of the additive manufacturing cost [12].

Table 2
Literature data about mechanical properties of additively-manufactured (AM) and wrought (WR) 316L stainless steels (σ_f represents the maximum fatigue stress).

Type	Condition	Ra [μm]	YS [MPa]	UTS [MPa]	E [GPa]	σ_f [MPa]	Run-out [cycles]	R [-]	Reference
AM	As-built	5–6	485	699	187	110	10^6	−1	[10]
AM	As-built	7.2	453	573	—	145	$2*10^6$	−1	[9]
AM	As-built	—	430–449	509–528	—	—	—	—	[8]
AM	As-built	—	441–517	529–633	—	—	—	—	[38]
AM	As-built	—	485–495	587–594	163–165	—	—	—	[7]
AM	As-built	—	220–640	520–760	—	—	—	—	[6]
AM	As-built	—	508–577	555–608	—	—	—	—	[5]
AM	As-built	—	588	622	—	—	—	—	[4]
AM	As-built	10.1	—	—	—	163	$2*10^6$	0.1	[22]
AM	As-built	—	—	581	—	—	—	—	[15]
AM	As-built	—	462	565	—	108	$2*10^6$	−1	[14]
AM	As-built	12.5	—	—	—	120	10^7	−1	[40]
AM	As-built	13.3	—	—	—	90	10^7	−1	[41]
AM	As-built	—	—	—	—	250	$5*10^5$	−1	[42,43]
AM	As-built	—	—	—	—	250	$2*10^5$	−1	[42,43]
AM	As-built + Machined	0.5	453	573	—	300	$2*10^6$	−1	[9]
AM	As-built + Machined	—	475	550	—	295	$3*10^5$	−1	[3]
AM	As-built + Machined	—	—	—	—	300–400	10^6	0.1	[12]
AM	As-built + Polished	—	—	—	—	145–180 (amplitude)	10^6	0.1	[2]
AM	As-built + Machined	—	—	—	—	165	10^7	−1	[19]
AM	As-built + Machined	—	640	760	—	255	10^7	0.1	[19]
AM	As-built + Polished	—	640	760	—	269	10^7	0.1	[19]
AM	As-built + Polished	< 1	511	621	—	101	10^7	−1	[44]
AM	As-built+ Polished	0.6	—	—	—	120–190	10^7	−1	[40]
AM	As-built+ Machined	1.2	—	—	—	140–220	10^7	−1	[40]
AM	As-built+ Polished	1.7	—	—	—	135	10^7	−1	[41]
AM	As-built+ Machined	1.1	—	—	—	165	10^7	−1	[41]
AM	As-built+ Polished	—	—	—	—	250	$7.5*10^5$	−1	[42,43]
AM	As-built+ Polished	—	—	—	—	338	$2*10^6$	−1	[42,43]
AM	As-built + Grinded	—	550–640	650–750		250–400	10^6	0.1	[13]
AM	As-built + Polished	0.8 (Rz)	—	—	—	320	10^6	−1	[11]
AM	As-built + Turned	—	462	565	—	267	$2*10^6$	−1	[14]
WR	Smooth	—	590	699	—	380	$5*10^6$	−1	[45]
WR	Smooth	—	345	563	187	350	10^5	−1	[10]
WR	Smooth	—	255–310	535–623	—	—	—	—	[7]
WR	Smooth	—	220–270	520–680	—	—	—	—	[5]
WR	Smooth	—	332	673	165	333	10^7	0.1	[20]
WR	Smooth	—	259	588	195	240	10^7	−1	[21]
WR	Smooth	—	262	586	—	269	10^7	−1	[46]
WR	Smooth	—	—	—	—	275–330	10^7	−1	[40]
WR	Smooth	—	—	—	—	350	$2*10^6$	−1	[42,43]

Laser remelting represents an alternative procedure to improve density of produced parts and reduce surface roughness [1,6,36,37]. This technique involves re-scanning of each powder layer twice before going to the next one. Nevertheless, laser remelting can dramatically reduce productivity [1,6]. Yasa and Kruth investigated the influence of laser remelting on components density [36]. This procedure improved surface quality reducing the average roughness, R_a, from 12 μm to 1.5 μm and the defects content was appreciably decreased from 0.77 % to 0.04 % [36]. In conclusion, such technique represents a possible alternative to conventional post treatments and it still preserves composition uniformity and refined microstructures [37].

AISI 316L is an austenitic chromium-nickel stainless steel widely adopted in various engineering fields, such as automotive, oil and gas, chemical and petrochemical industries, because of its good ductility, mechanical strength and corrosion resistance [2–5,7–9,11–16,20–22,36,38,39]. As reported in literature, SLMed 316L stainless steel can provide higher tensile strength in comparison to conventionally-produced wrought parts thanks to the presence of refined microstructures and higher dislocation densities [1,3–5,7–9,13–15,20,22]. However, the ductility of SLMed materials is generally lower than in wrought counterparts. Stern et al. investigated the fatigue behavior of SLMed 316L stainless steel observing that uniaxially tested specimens almost always had crack initiation sites close to the surface [11]. In addition, they stated that porosity is not necessarily detrimental to fatigue performance, but large and sharp defects close to the surface represents strong stress concentrators [11]. According to Riemer et al., defects in SLMed 316L stainless steel are not so detrimental to the high cycle fatigue behavior because this material shows high ductility [14]. For this reason, 316L stainless steel is considered highly defect- and residual stress- tolerant [4,11,14]. Considering such high defect tolerance induced by the excellent ductility of austenite, expensive post treatments may be omitted and components could be also

Table 3
Summary of data reported in Table 2 with average values and ranges of tensile properties, fatigue limits and fatigue ratii referred to $R = -1$ (AM: additive manufacturing; WR: wrought).

Type		YS [MPa]	UTS [MPa]	σ_f [MPa]	$\frac{\sigma_f}{UTS}$
AM (as-built)	Average	486	595	112	0.19
	Range	220–640	509–760	90–145	0.15–0.25
AM (as-built + post proc.)	Average	525	624	218	0.39
	Range	453–640	550–760	101–320	0.20–0.54
WR (smooth)	Average	342	617	285	0.44
	Range	220–590	520–699	236–380	0.35–0.54

directly put in service in the as-built condition [4,11,14]. In fact, the authors did not observe any appreciable improvement in fatigue limits with post processing techniques aimed at increasing the overall component quality. Similarly, HIP and stress relieving did not provide any substantial increase of fatigue strength [13]. So, it is expected that defects are not so detrimental to fatigue performance and this characteristic could allow exploiting higher processing speeds with enhanced industrial productivity [12]. In fact, despite the internal defects content should impact fatigue properties also in the machined condition, Andreau et al. identified no clear influence on fatigue limits of different defects fractions and distributions [12].

In comparison to wrought components, the as-built SLMed condition is associated to reduced fatigue limits because of internal and surface defects. Considering data available in literature, Table 2 reports a detailed summary of the mechanical properties of additively-manufactured and wrought 316L stainless steels. Table 3 provides a comparison between additive and conventional wrought materials reporting average values about tensile properties and fatigue limits with different load ratii. According to literature data, post processing techniques aimed at improving surface roughness and removing near surface defects provide a slight increase in fatigue limits and fatigue ratii. Regarding conventional wrought materials, there is a slight increment of the average fatigue limit, while the average fatigue ratio is very similar to that observed in additively-manufactured materials with improvements in surface quality. So, to be comparable with conventional wrought parts in terms of fatigue performance, SLMed components necessarily require post-processing operations to remove the defects-rich surface layer and roughness.

This research work investigates the influence on the fatigue behavior of post-processing surface improvements. In fact, the fatigue limit in the as-built condition is compared to that obtained removing by grinding the defects-rich surface layer and improving the surface roughness. Then, fatigue limits and failures were investigated from the perspective of fracture mechanics principles. Each broken fatigue specimen was analysed by SEM and the killer defects were characterized in terms of equivalent micro-notch length according to the Murakami's approach [47]. Each fatigue failure observed in this experimental work was investigated using the Kitagawa-Takahashi diagram to relate the applied fatigue stress and the equivalent total micro-notch length. In this case, the limit curve for non-propagating cracks was defined according to different models available in literature. In particular, a comparison between the El-Haddad and Chapetti models was performed to confirm the non-conservativeness of the first approach. Then, considering the equivalent micro-notch at 50 % probability in fatigue specimens, the experimental Wöhler fatigue limits were better analysed using the K-T diagram.

Table 4
Surface roughness (average and standard deviation) of SLMed fatigue specimens in both the as-built and contour-free conditions (Ra: average value of all the fatigue specimens; Rt, Rz, Rv, Rc: average of maximum values in each fatigue specimen).

Condition	Ra [µm]	Rt [µm]	Rz [µm]	Rv [µm]	Rc [µm]
As-built (average)	7.1	55.2	42.3	24.1	22.4
Contour-free (average)	0.05	0.8	0.4	0.2	0.1
As-built (dev.st)	0.8	2.2	3.6	2.2	2.0
Contour-free (dev. st)	0.02	0.4	0.2	0.1	0.1

2. Materials and method

316L stainless steel specimens for fatigue and tensile tests were fabricated by LPBF technique with process parameters already optimized by the manufacturer. Cylindrical specimens for rotating-bending fatigue testing were manufactured vertically according to standard ISO 1143:2021 with a diameter of 6 mm [48]. The drawing of the fatigue specimens is reported in Fig. 1.

Rotating-bending fatigue behavior was investigated in both the as-built and contour-free conditions. Fatigue limits were determined with the stair-case method, according to standard ISO 12107:2012 [49]. Contour-free specimens were obtained removing the outer layer of approximately 260 µm thickness. This operation was performed by grinding with subsequent polishing. Both the operations were carried out manually with grinding papers (from 80-grit to 1200-grit) and 3 µm diamond cloth. They were performed along the specimen axis to prevent detrimental circumferential scratches. Moreover, polishing was carried out carefully to avoid localized plasticization. In each specimen, the surface roughness was measured by a Taylor-Hobson contact profilometer, according to standard ISO 21920-2:2022 [50]. The data reported in Table 4 are obtained from nine measurements performed along the axis of each fatigue specimen in the straight zone.

Room-temperature tensile properties were investigated by tensile tests according to standard ISO 6892 [51] considering specimens manufactured vertically with dimensions of 6 mm diameter, 25 mm cylindrical length and 12.5 mm extensometer gauge length. HV2 hardness tests were performed according to standard ISO 6507 [52]. Then, both the as-built and contour-free conditions were analysed by light-optical and scanning-electron (LOM and SEM) microstructural observation. Size, morphology, position and distribution of defects were characterized by image analysis on optical micrographs considering the classification procedure described by the Murakami's theory [23,47]. Surface and internal defects were characterized determining the $\sqrt{area}$ size parameter. According to the Murakami's method [23,47], the $\sqrt{area}$ size

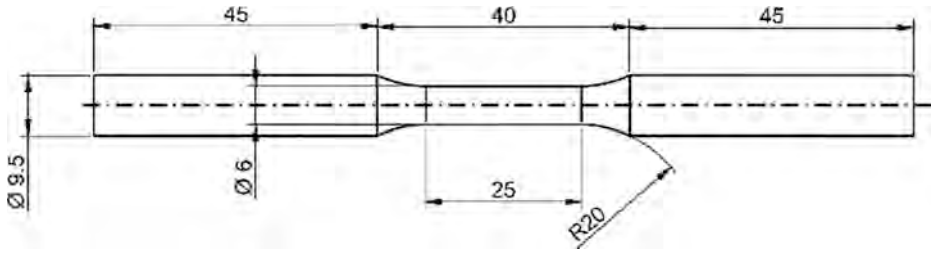

Fig. 1. Drawing of the fatigue specimens adopted in this work.

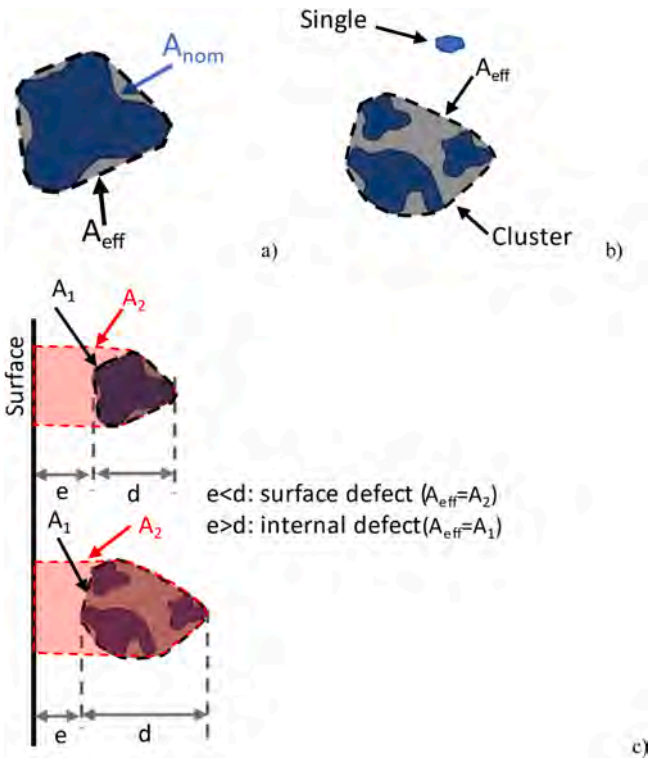

Fig. 2. Procedure to determine the convex effective area of single defects (a) and cluster of defects (b) with and without presence of defect-surface interaction (c).

parameter represents the effective length of the equivalent flaw calculated from the convex defect area which was determined manually. In the presence of a single defect, the convex defect area is calculated considering the enveloping contour shape, as shown in Fig. 2.a. When multiple defects are present, interaction among them should be carefully investigated. A cluster is obtained when distances between adjacent defects are lower than the equivalent diameter of the smallest defect in the cluster, as shown in Fig. 2.b. In the case of a cluster, it is characterized considering the convex area which envelopes all the cluster-contained defects. Successively, the Murakami's approach analyses the interaction of sub-surface defects with the surface [47]. When the defect-to-surface distance exceeds the defect size, no defect-surface interaction is present, as shown in Fig. 2.c.

In the presence of surface shallow defects, such as surface roughness and surface defects with length-to-width ratio $l/w \geq 10$, the equivalent flaw effective length is determined considering the defect depth, t, as described by the Murakami's approach [47]. In this case, the $\sqrt{area}$ size parameter is determined using Equation (1).

$$\sqrt{area} = \sqrt{10}t \tag{1}$$

For the surface roughness, the conversion into an equivalent micro-notch is performed considering the Murakami's approach [47]. Since this defect type is continuously distributed along the entire surface, it can be considered as a shallow defect and its depth is approximately equal to the R_v roughness parameter [53–55].

Specimens were obtained in both transversal and longitudinal directions from the heads of fatigue samples. Metallographic preparation was performed according to conventional techniques characterized by mounting in thermosetting phenolic resin followed by grinding and polishing. Chemical etching was done using a solution recommend by standard ASTM E407 [56]. Fracture surfaces of fatigue specimens were investigated using SEM to determine micro-mechanisms of fatigue failures. Then, also the size parameter $\sqrt{area}$ of killer defects was measured in each observed condition to analyse the relation with the applied stress.

Successively, fatigue limits and failures were better analysed from the perspective of fracture mechanics principles. In each condition, the applied stress-intensity factor K was determined considering the applied nominal stress σ and the total equivalent micro-notch length of defects. Specifically, El-Haddad et al. [57] studied the correlation between the ΔK threshold (ΔK_{th}) and the fatigue limit ($\Delta\sigma_f$). They defined an intrinsic crack, a_0, which summarizes the effects of all the existing defects. The Kitagawa-Takahashi diagram shown in Fig. 3.a describes the relationship among fatigue stress, ΔK threshold and crack length [58]. The parameter a_0 reported in Equation (2) is the intrinsic crack representative of all the microscopic defects, such as non-metallic inclusions, lattice defects, micro-cracks and process-related damages.

$$a_o = \frac{1}{\pi}\left(\frac{\Delta K_{th,LC}}{Y\Delta\sigma_f}\right)^2 \tag{2}$$

where $\Delta K_{th,LC}$ is the ΔK threshold for long cracks and $\Delta\sigma_f$ is the fatigue limit.

However, when cracks are not associated to a complete crack closure build-up, especially in the case of short cracks, the ΔK threshold is reduced compared to that of long cracks [59,60]. In this condition, the El-Haddad approximation is non-conservative and the Chapetti's model [61] can be adopted to account for this behavior, as shown in Fig. 3.b. The non-propagating Chapetti region shown in Fig. 3.b is defined by the limit curve associated to the intrinsic (effective) $\Delta K_{th,eff}$ threshold. In the literature, the crack closure build-up is described using different methods based on exponential or other types of functions. All these

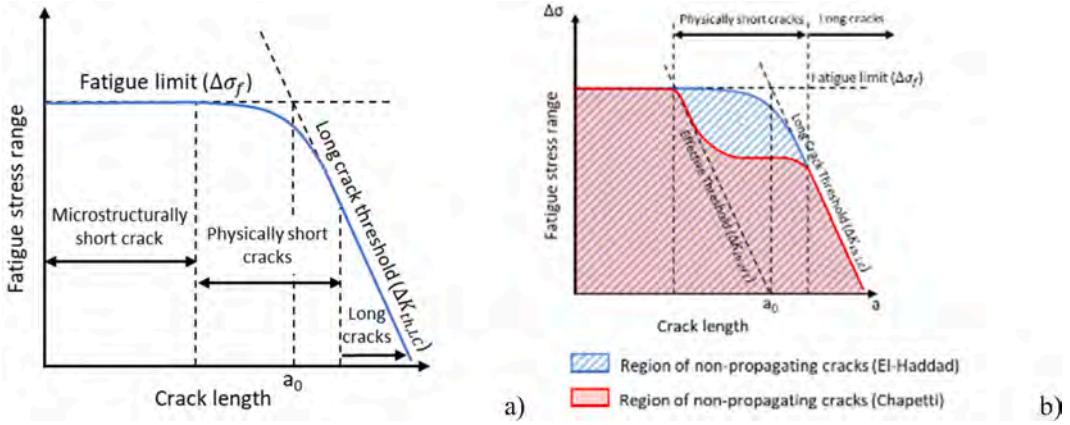

Fig. 3. a) Kitagawa-Takahashi diagram showing the relationship among fatigue stress range, ΔK threshold and crack length; b) Comparison between the regions of non-propagating cracks according to different approaches.

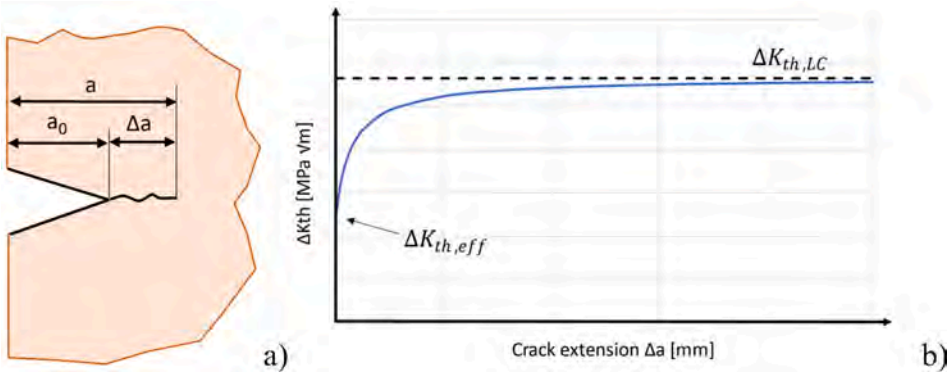

Fig. 4. Crack growth resistance curve (R-curve) as a function of crack extension.

approaches are defined to reach the long crack ΔK_{th} threshold asymptotically [61–63]. Additionally, Tanaka and Akiniwa demonstrated that the region of non-propagating cracks is reduced with increasing initial defect length [60]. As a result, the crack growth resistance curve, also called R-curve, was defined to evaluate the relationship between ΔK threshold and crack length, as shown in Fig. 4.b.

The intrinsic (effective) ΔK threshold, $\Delta K_{th,eff}$, is exclusively a function of the material physical properties and it does not depend neither on the microstructure nor the load ratio. Its value can be determined using different expressions available in the literature. Equation (3) shows the model reported by Li et al. [64] to determine the intrinsic (effective) ΔK threshold. It depends on the elastic modulus, E, the Burgers vector, $\boldsymbol{b}$, and α, which is equal to 1 according to Hertzberg [65] or 0.75 according to Pippan et al. [66]. The Burgers vector is defined by Equation (4) and it is a function of the lattice parameters.

$$\Delta K_{th,eff} = \alpha\sqrt{|\boldsymbol{b}|E} \tag{3}$$

$$|\boldsymbol{b}| = \frac{a}{2}\sqrt{h^2+k^2+l^2} \tag{4}$$

where a is the unit cell edge length, while h, k and l are the Burgers vector components. In the FCC lattice, the $\langle 1,1,0\rangle$ family of directions includes the most common sliding directions, hence $|\boldsymbol{b}| = \frac{a}{2}\sqrt{2}$.

As previously described, the El-Haddad limit curve reported in Equation (5) is non-conservative. For this reason, other authors slightly modified the El-Haddad model to account for the ΔK_{th} variation with the crack length in the crack growth resistance R-curve [61,67]. This model for the limit curve is shown in Equation (6).

$$\Delta\sigma_{th} = \frac{\Delta K_{th,LC}}{Y\sqrt{\pi(a+a_o)}} \tag{5}$$

$$\Delta\sigma_{th} = \frac{\Delta K_{th}(a)}{Y\sqrt{\pi(a+a_o)}} \tag{6}$$

A different expression for the limit curve is reported in Equation (7). In this case, the El-Haddad parameter a_0 is substituted by $a_0^{'}$, whose expression is shown in Equation (8).

$$\Delta\sigma_{th} = \frac{\Delta K_{th}(a)}{Y\sqrt{\pi(a+a_o^{'})}} \tag{7}$$

$$a_o^{'} = \frac{1}{\pi}\left(\frac{\Delta K_{th}(a)}{Y\Delta\sigma_f}\right)^2 \tag{8}$$

In this analysis, the crack growth resistance R-curve is estimated considering the model defined by Zerbst et al. [63] and reported in Equation (9).

$$\Delta K_{th} = \Delta K_{th,LC}\sqrt{\frac{\Delta a + a^*}{\Delta a + a^* + a_o}} \tag{9}$$

$\Delta K_{th,LC}$ is the ΔK threshold in the case of long cracks and a_0 is the El-Haddad intrinsic crack length. The additional parameter a^* is adopted to obtain $\Delta K_{th} = \Delta K_{th,eff}$ when $\Delta a = 0$. This parameter is defined by Equation (10).

$$a^* = a_o\frac{(\Delta K_{th,eff}/\Delta K_{th,LC})^2}{1-(\Delta K_{th,eff}/\Delta K_{th,LC})^2} \tag{10}$$

3. Results and discussion

3.1. Metallographic analysis of microstructures and defects

Fig. 5 shows the micrographs of transversal and longitudinal sections in both the as-polished and etched conditions with different magnifications at LOM and SEM. In addition, details of the typical process-induced defects, such as lack-of-fusion pores and gas porosities, are shown in Fig. 5. In the transversal plane, microstructural observation revealed presence of elongated tracks of the melt pools with almost perpendicular directions due to the laser-scanning rotation in the layer-stacking process. The outer contour layer is characterized by a different microstructural morphology because of the presence of distinct scanning parameters. This difference is responsible for the increased density of defects in comparison to inner regions. Lack-of-fusion pores are prevalently positioned close to the surface and they show irregular shapes. On the contrary, inner zones are mainly characterized by gas porosities with almost spherical morphology, as shown in Fig. 5. In the longitudinal plane, melt pools are stacked in the build direction with almost uniform orientation and shape, as shown in Fig. 5.e. The solidification microstructure reported in Fig. 5.f is clearly evident at SEM and it is characterized by presence of both a cellular-shaped structure and elongated dendrites with different orientations. The average size of the intragranular cells shown in Fig. 5.f is approximately equal to 1 μm diameter. The average percentage fraction of defects in the as-built condition is equal to 1.45 %. As shown in Fig. 5.e, the scanning technique produces periodic melt pools deposited layer by layer. They are very similar to several aligned welding beads whose boundaries are clearly highlighted by etching. The dimensions of such melt pools were measured on optical micrographs at 100X resulting in an average depth of 80 μm and width of 150 μm.

Contour-free fatigue specimens were obtained removing by grinding a radial thickness of 260 μm. This procedure allowed to eliminate the external defects-rich region which contained lack-of-fusion pores, especially. Fig. 6 shows the transversal section of contour-free fatigue specimens in both the as-polished and etched conditions. Some internal porosities were still present and they mainly consisted of spherical pores induced by entrapped gas. In this case, the average percentage fraction

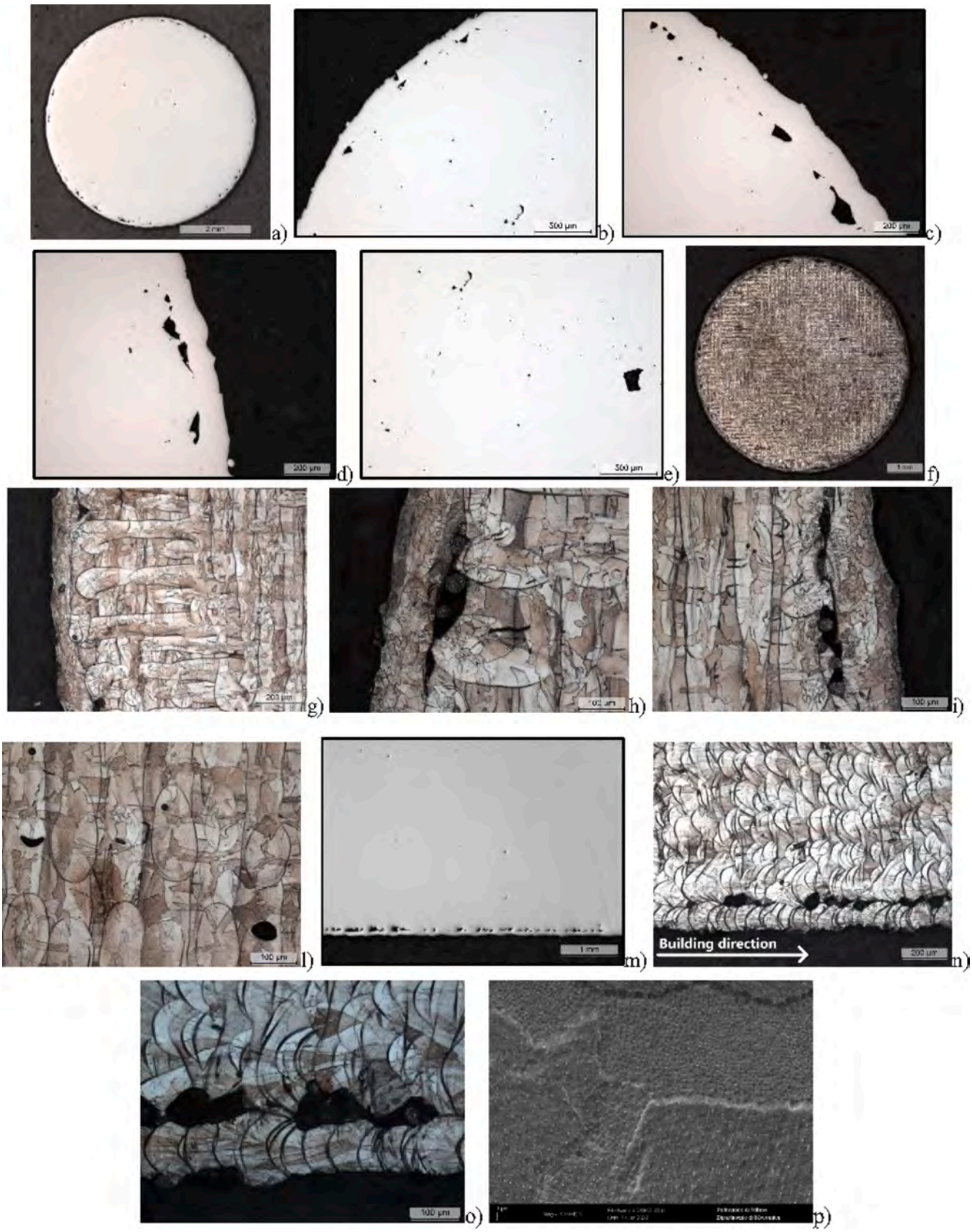

Fig. 5. As-built specimens: microstructures observed in transversal (a, b, c, d, e, f, g, h, i, l) and longitudinal (m, n, o) planes in both the as-polished and etched conditions. SEM micrograph in the transversal plane (p).

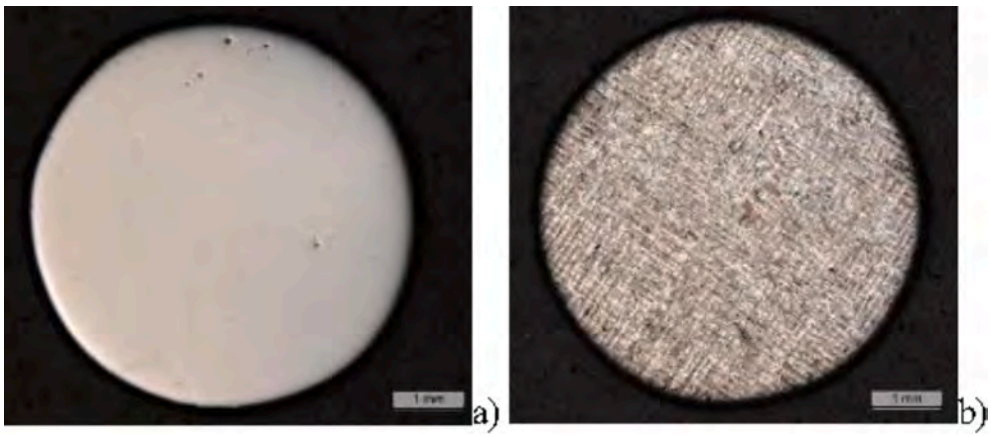

Fig. 6. Transversal section of contour-free fatigue specimens in both the as-polished and etched conditions.

of defects is equal to 0.20 %.

Metallographic analysis of defects in the as-built condition was performed considering transversal sections from different fatigue specimens. A significant amount of defects was mainly observed in the near surface layer. The thickness of the external defects-rich layer ranges from 100 μm to 200 μm. Such defects, mainly associated to lack of fusion and presence of entrapped gas, were characterized by image analysis in terms of size, position, morphology and distribution. Fig. 7.a and Fig. 7.b describe the distribution of defects in the as-built condition considering size and roundness as a function of the radial distance from the surface. The defect size was evaluated considering the classification procedure of the Murakami's theory which is based on the parameter $\sqrt{area}$ [23,47]. The morphology of such defects was deeply investigated also calculating the roundness parameter, shown in Equation (11), where A is the area and p is the perimeter of the defect. When this parameter has a value equal to 1, it indicates a perfect circle. As the value increases, it indicates an increasingly irregular shape. Generally, gas porosities are characterized by roundness close to 1 because of pressure uniformity, while lack-of-fusion defects typically show irregular shapes with roundness values even significantly higher than 1.

$$Roundness = \frac{p^2}{4\pi A} \tag{11}$$

The majority of defects is located at the surface and in the near surface layer, while inner zones show a reduced amount. Moreover, internal defects are smaller and their size parameter does not exceed 100 μm. Instead, surface defects are present with size parameter up to 250 μm. These results confirm that the contour layer is the most critical in terms of defects amount and severity. In fact, the largest defects are positioned close to the surface where local stresses are generally higher. In addition, as shown in Fig. 7.b, the highest roundness values occur near the surface indicating that such region contains defects that are not only the largest, but also the most irregular ones. As shown in Fig. 7.a, in contour-free fatigue specimens, an external layer of 260 μm thickness was removed by grinding operations. However, after this procedure, internal defects can become surface porosities, but their size parameters are reduced compared to those observed in the original surface layer. Fig. 7.e shows the percentage probability of defect presence in each radial interval as a function of the distance from the surface. Considering the average thickness (260 μm) removed by grinding in contour-free fatigue specimens, the probability of defect presence in the radial interval, 200 μm to 400 μm, from the surface still remains high and equal to 97 %. Moreover, an increase in the grinding depth does not provide any appreciable improvement since subsequent distance ranges still show really high probability values. According to these results, even after deep grinding operations, it is very difficult to obtain completely defect-free surfaces. In fact, despite the probability of defect presence reduces increasing the distance from the surface, its values still remain significant. The overall surface-to-core radial range is populated at 56 % in average by defects. Fig. 7.c compares the relationship between roundness and size parameter for both surface and inner defects. Fig. 7.d investigates the size parameter distributions for both inner and surface defects. In both cases, the experimental data were fitted by log-normal distributions leading to the fitting parameters reported in Fig. 7.d. Fig. 7.f shows the cumulative percentage of fatigue specimens with respect to the maximum defect size ($\sqrt{area}$) observed in each of them. It describes the percentage of fatigue specimens with maximum defect size lower than a certain value. For instance, 10 % of the fatigue specimens have a maximum defect size lower than 138 μm, 50 % lower than 188 μm and 90 % lower than 238 μm. Considering that the technical literature states that the maximum defect size determines the fatigue resistance, the value observed in 50 % of the fatigue specimens, 188 μm, can be adopted to estimate the Wöhler fatigue limit at 50 % survival probability. Similarly, the fatigue limits with different survival probability can be obtained considering the cumulative percentages reported in Fig. 7.f. For instance, 90 % of the fatigue specimens have defects smaller than 238 μm. To be sure that all these specimens survive the fatigue tests, it is necessary that the applied stress is lower than that associated to a maximum defect size of 238 μm.

3.2. Mechanical properties

The mechanical properties in the SLMed material are reported in Table 5. The presence of excellent properties in the as-built condition is primarily associated to the marked microstructural refinement induced by the high cooling rates of the SLM process. Furthermore, the mechanical properties in the as-built condition are very similar to those reported in literature for SLMed components and summarized in Table 3.

Regarding hardness, Bartolomeu et al. compared 316L stainless steel produced with different techniques: conventional casting, hot pressing and SLM process [39]. The authors identified average hardness values equal to 160 HV, 175 HV and 225 HV, respectively. Tolosa et al. observed an average hardness of 235 HV in SLMed material [5]. Shamsujjoha et al. identified a slightly lower value equal to 200 HV [4]. So, hardness in as-built specimens lies within the range defined by literature data. Moreover, thanks to the presence of a refined microstructure, it is significantly higher than that observed in conventionally-cast components.

3.3. Fatigue tests: Fatigue limit and S-N Wöhler diagram

Then, rotating-bending fatigue tests were performed at room temperature with load ratio $R = -1$ on cylindrical specimens in both the as-

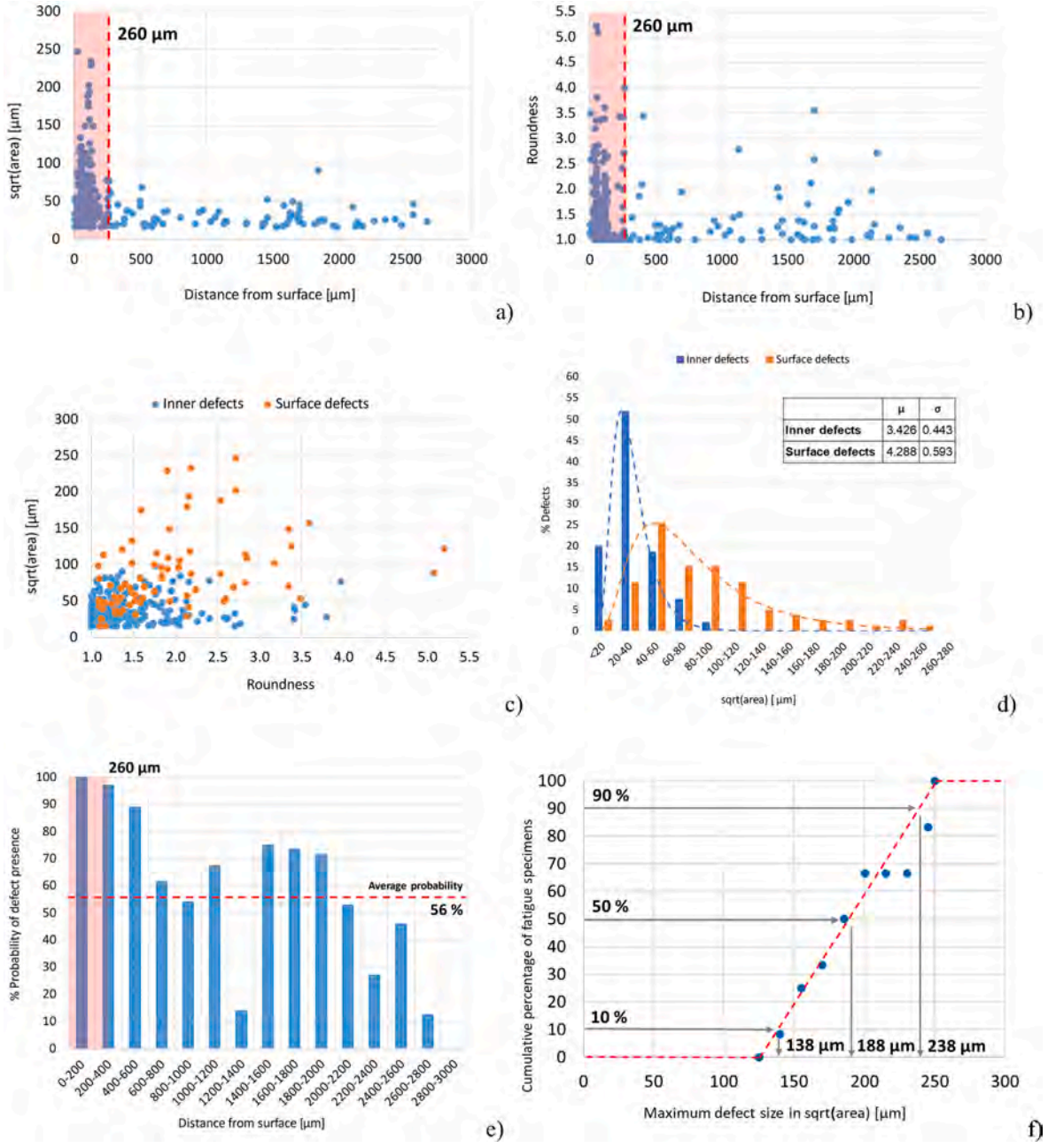

Fig. 7. Defects size, morphology, position and distribution in the as-built condition. The red area indicates the radial thickness removed by grinding from as-built fatigue specimens to obtain the contour-free ones. a) Size parameter $\sqrt{area}$ of surface and inner defects as a function of the distance from the surface; b) Roundness of surface and inner defects as a function of the distance from the surface; c) Relation between size parameter and roundness compared for surface and inner defects; d) Distribution of size parameter for surface and inner defects and log-normal distribution fitting; e) Percentage probability of defect presence in each radial interval and average value; f) Percentage of fatigue specimens with maximum defect size lower than a certain value. (For interpretation of the references to colour in this figure legend, the reader is referred to the web version of this article.)

Table 5
Room-temperature mechanical properties of SLMed as-built specimens. Hardness tests were performed on both transversal and longitudinal sections considering three measurements on each sample adopted for the metallographic analysis.

HV2 (L)	HV2 (T)	YS [MPa]	UTS [MPa]	YS/UTS [-]
242	229	442	591	0.75

built and contour-free conditions, according to standard ISO 1143:2021 [48]. Experimental tests were done considering a test frequency of 50 Hz and run-out condition equal to 10^7 cycles. The fatigue limit was determined with the stair-case method, according to standard ISO

Table 6
Comparison between the rotating-bending fatigue limits ($R = -1$) in the as-built and grinded (contour-free) conditions.

Condition	σ_f [MPa]	σ_f/UTS
SLM – As-built	120	0.20
SLM – As-built (contour-free)	150	0.25

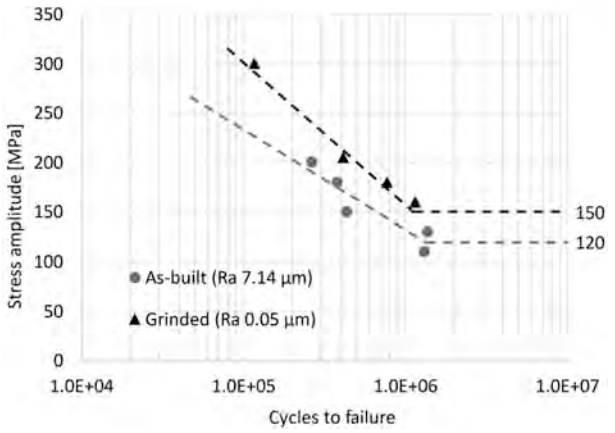

Fig. 8. S-N Wöhler diagram in both the as-built (Ra 7.14 µm) and grinded contour-free (Ra 0.05 µm) conditions.

12107:2012 [49]. Stair-case tests were performed considering a stress increment, $\Delta\sigma$, equal to 20 MPa. According to the experimental results, the fatigue limit in the as-built condition is equal to 120 MPa, while it increases at 150 MPa in the contour-free specimens.

A summary of the fatigue limits is given in Table 6. According to the results, the surface coefficient, b_2, adopted to calculate effective fatigue limits from theoretical ones, is determined equal to 0.80 according to the expression reported in Equation (12). Considering the yield strength-to-UTS ratio and the surface roughness,R_t, of as-built SLMed specimens, this value is in good agreement with literature data [68]. This observation confirms that presence of a poor surface quality in as-built SLMed components does not provide severe reduction of fatigue limits thanks to the high ductility of this material which allows good defect tolerance. Moreover, as also observed by metallographic analysis, the probability of defects presence in the surface layer of grinded fatigue specimens still remains very high despite the removal of the original contour region. So, the presence of a marginal increment in fatigue limit after such grinding procedure is also determined by the almost unavoidable presence of surface defects. In fact, as shown by the SEM analysis of fracture surfaces, fatigue nucleations in stair-case specimens were always obtained from surface lack-of-fusion defects. Improvements obtained by grinding and polishing are associated to the removal of the largest defects and better surface finishing.

$$b_2 = \frac{\sigma_{f(as-built)}}{\sigma_{f(grinded)}} \tag{12}$$

In the as-built SLMed condition, the ratio between the fatigue limit and UTS is compatible with the literature database reported in Table 3. However, grinded SLMed specimens showed a reduced improvement in fatigue strength compared to the literature data which show a higher average value. Despite such slight increment, the observed fatigue ratio still lies within the literature range for mechanically post-processed

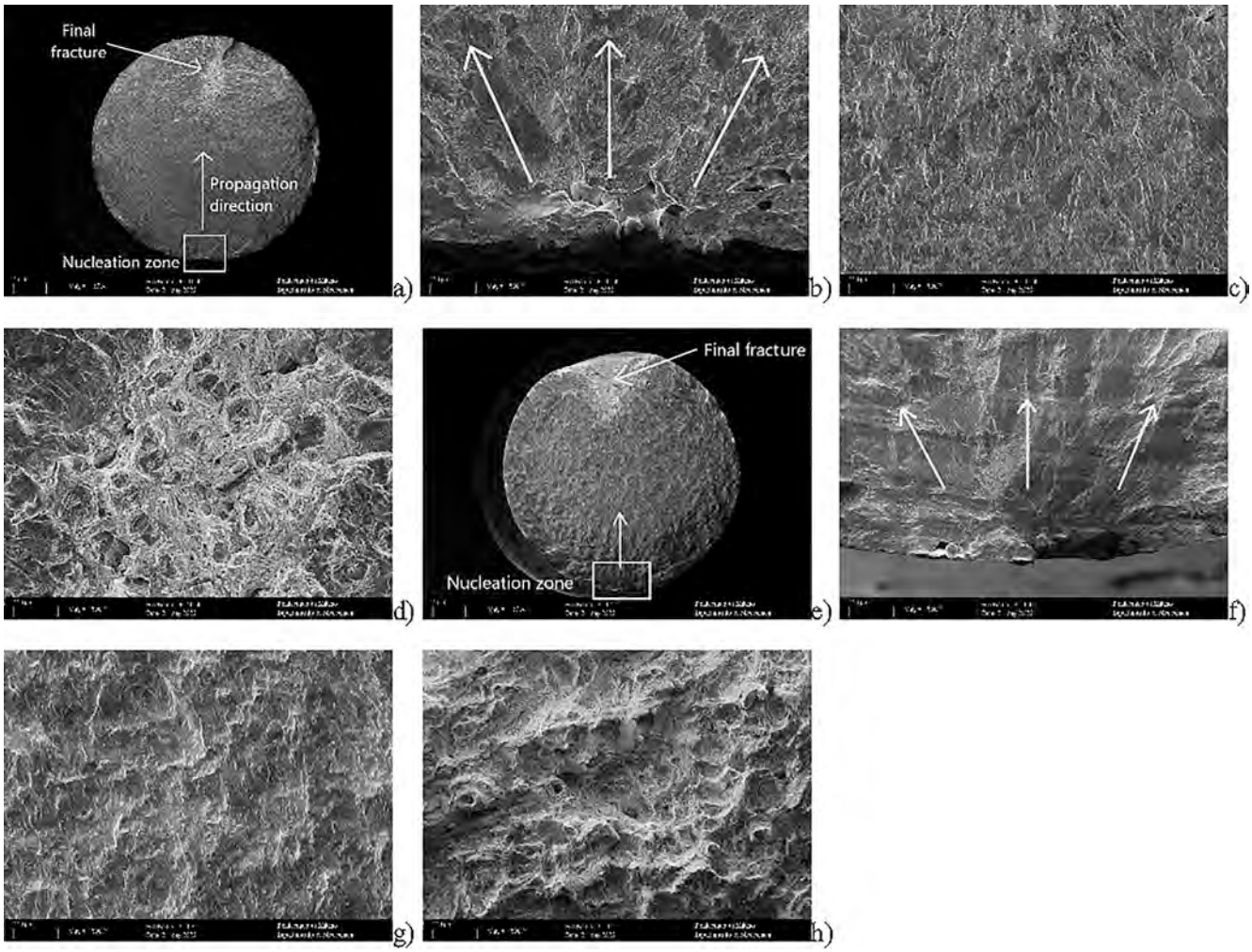

Fig. 9. SEM micrographs of the fracture surfaces of some fatigue specimens. Images are reported in this order for each sample: overview, nucleation zone, propagation zone and final fracture. Sample D (a, b, c, d); Sample I (e, f, g, h).

Table 7
Size parameter $\sqrt{area_{eff}}$ of killer defects, micro-notch associated to the roughness and roundness of killer defects for the broken fatigue specimens. Results obtained by image analysis on SEM micrographs. The depth is reported only in the case of shallow surface defects. This analysis was performed according to the Murakami's theory [23,47].

ID	Condition	σ_a [MPa]	Cycles to failure	Nucleation	Roundness	Shallow (YES/NO)	Depth [μm]	$\sqrt{area_{eff}}$ [μm]	Micro-notch (roughness) [μm]	Micro-notch total length [μm]
A	As-built	110	1.300.000	Surface (LoF)	2.17	NO	—	271	76	347
B	As-built	130	1.300.000	Surface (LoF)	1.74	NO	—	174	76	250
C	As-built	130	1.400.000	Surface (LoF)	1.35	NO	—	178	76	254
D	As-built	130	1.384.000	Surface (LoF)	1.85	NO	—	189	76	265
E	As-built	150	433.000	Surface (LoF)	2.54	NO	—	285	76	361
F	As-built	180	380.000	Surface (LoF)	4.08	YES	62	196	76	272
G	As-built	200	264.393	Surface (LoF)	2.24	NO	—	358	76	434
H	Grinded	160	928.200	Surface (LoF)	1.96	NO	—	114	76	190
I	Grinded	160	526.540	Surface (LoF)	4.16	NO	—	153	76	229
L	Grinded	160	1.980.789	Surface (LoF)	4.81	YES	82	259	76	335
M	Grinded	180	770.600	Surface (LoF)	1.24	NO	—	70	76	146
N	Grinded	205	411.111	Surface (LoF)	2.56	NO	—	67	76	143
O	Grinded	300	116.600	Surface	—	—	—	—	76	76

specimens reported in Table 3. The improvement in fatigue limit obtained by grinding of AM fatigue specimens is equal to 25 %. Even though such increment is limited by the unavoidable presence of surface defects even after grinding, the percentage increase in fatigue strength is satisfying. In fact, the removal of the surface layer allowed elimination of the worst defects in terms of size and morphology. However, as shown in Fig. 7.e, even after deep grinding operations, it is really unlikely to obtain completely defect-free surfaces. This condition limits further increment of fatigue strength since rotating bending exposes uniformly each surface point to cyclic tensile/compression stresses. Moreover, referring to Fig. 7.c, pores that can become surface defects in the contour-free condition are really sharp because of roundness values up to 4. According to this observation, SEM analysis demonstrated that broken grinded fatigue specimens still have crack nucleation from surface lack-of-fusion defects.

Then, after the analysis of fatigue limits, experimental tests in the finite-life region were also performed to determine the S-N Wöhler diagrams, as shown in Fig. 8.

As reported in the literature [40–43,70], the 3D-printing machine, the process parameters, such as atmosphere, platform temperature, scanning speed and hatch spacing, the powder characteristics have great influence on fatigue life. For instance, in both the as-built and grinded conditions, the fatigue limits and S-N curves found in this paper are generally lower than those found in [42,43]. Nevertheless, in the as-built condition, such difference decreases if compared to the results obtained with the specimens fabricated by the 3D-printing machine B [42,43]. In addition, considering literature data reported in [40,41,70], the fatigue limits and S-N curves obtained in this research work and presented in Table 6 and Fig. 8 are in good agreement.

3.4. SEM analysis of fatigue fracture surfaces and killer defects

Then, the fracture surfaces were investigated by SEM to determine the micro-mechanisms associated with the fatigue failure. Crack nucleation, propagation region and final fracture are detected and highlighted in the SEM micrographs shown in Fig. 9. Table 7 reports a detailed characterization of killer defects at the nucleation site for each broken specimen. In both the as-built and grinded fatigue specimens, crack nucleation occurred at the outer surface because of lack-of-fusion pores except for a single grinded specimen where fatigue nucleation was obtained from surface roughness. In some conditions, also multiple nucleation was observed. Since the combined presence of near-surface porosity and roughness is more critical compared to the presence of a single flaw only, it is necessary to define an equivalent micro-notch length which combines the effects of near-surface defects and roughness, represented by the parameter *Rv*, as suggested in the literature [55]. In this research work, to consider the overall effect of the two flaw kinds, the authors proposed to add the equivalent micro-notches, as done in the last column of Table 7. The final fracture zone is characterized by presence of small dimples related to a micro-ductile mechanism. Fig. 10 reports some examples of the calculation of the size parameter on fatigue fracture surfaces obtained by SEM analysis.

3.5. Analysis of fatigue limits and failures based on R-curve and K-T diagrams

As described, such defects directly affect the fatigue limit of the material. In this work, considering them as equivalent flaws, fracture mechanics principles are adopted to better investigate fatigue behavior. In the presence of a defect, according to the Murakami's approach [47], the applied stress-intensity factor K with nominal stress σ is given by Equation (13).

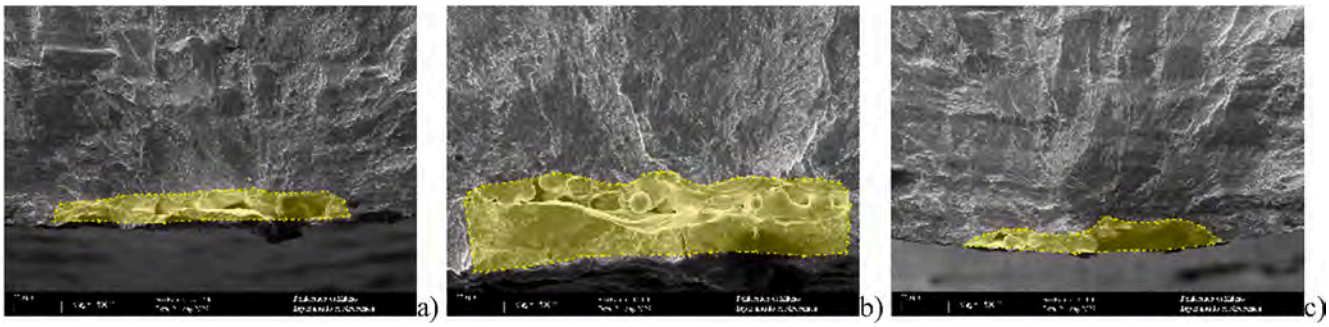

Fig. 10. Calculation of the size parameter of killer defects according to the Murakami's theory [23,47]. a) Sample F; b) Sample G; c) Sample I.

Table 8
Calculated $\Delta K_{th,eff}$ and $\Delta K_{th,LC}$ values for 316L stainless steel.

$\Delta K_{th,eff}$ [MPa$\sqrt{m}$]	$\Delta K_{th,LC}$ [MPa$\sqrt{m}$]	$\Delta K_{th,LC}$ (Murakami) [MPa$\sqrt{m}$]
2.5	11.3	11.6

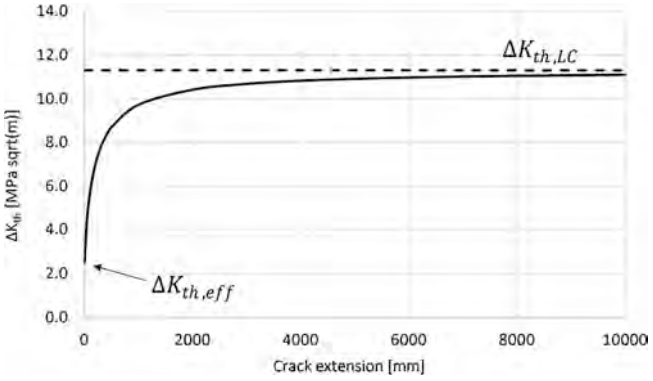

Fig. 11. Influence of the crack extension on the ΔK threshold.

$$K = \sigma Y \sqrt{\pi \sqrt{area}} \tag{13}$$

The constant Y is equal to 0.65 and 0.50 for surface and internal defects, respectively. The $\sqrt{area}$ size parameter is determined for each defect according to the Murakami's approach [47]. The stress-intensity factor K is really important because it is a function of the shape, dimension and position of each defect.

The intrinsic (effective) $\Delta K_{th,eff}$ threshold was calculated using Equation (3). Its average value, reported in Table 8, is in good agreement with literature data [71]. The $\Delta K_{th,LC}$ threshold was determined considering literature data at negative load ratii. In particular, as demonstrated in the literature, the $\Delta K_{th,LC}$ threshold at load ratio $R = -1$ can be obtained by linear extrapolation of experimental data at positive load ratii [54,72–77]. The reference values for 316L stainless steel were collected and averaged from several authors [47,73,75]. The calculated $\Delta K_{th,LC}$ threshold is in good agreement with the value obtained evaluating the Murakami's formula, reported in Equation (14), at $\sqrt{area}$ equal to 1000 μm, which represents the threshold between the short and long crack regions according to the author [47].

$$\Delta K_{th} = 0.0033(HV + 120)\left(\sqrt{area}\right)^{1/3} \tag{14}$$

HV is the Vickers hardness reported in Table 5. The value of $\Delta K_{th,LC}$ threshold considered in this analysis is reported in Table 8. Then, the influence of the crack extension on the ΔK threshold is reported in Fig. 11.

To define the K-T diagram, it is necessary to determine the theoretical fatigue limit (σ_{f0}) in the absence of the SLM intrinsic defects. For this reason, in this work, as reported in the Introduction, a wide literature review was performed to collect a database of fatigue limits for conventional 316L stainless steel determined on smooth fatigue specimens. In particular, according to the literature, fatigue limits can also be estimated as a fraction of UTS. For conventional ductile steels, the ratio between the fully-reversed rotating-bending fatigue limit ($R = -1$) and UTS ranges from 0.4 to 0.6. According to the literature database summarized in Table 3, this ratio varies between 0.35 and 0.54 and the average value, equal to 0.44, is adopted to determine the theoretical fatigue limit (σ_{f0}) for the SLMed material which is equal to 260 MPa (stress amplitude). Adopting this value in Equation (2), the El-Haddad intrinsic crack becomes equal to 355 μm.

The limit curves in the K-T diagram determined according to Equations (5), 6 and 7 are shown and compared in Fig. 12.a. In the following analysis, the limit curve defined by Equation (7) is selected as the reference model. The limit curve for non-propagating cracks depends on the crack length of the equivalent micro-notch determined according to the Murakami's approach [47]. Fig. 12.b compare the limit curves

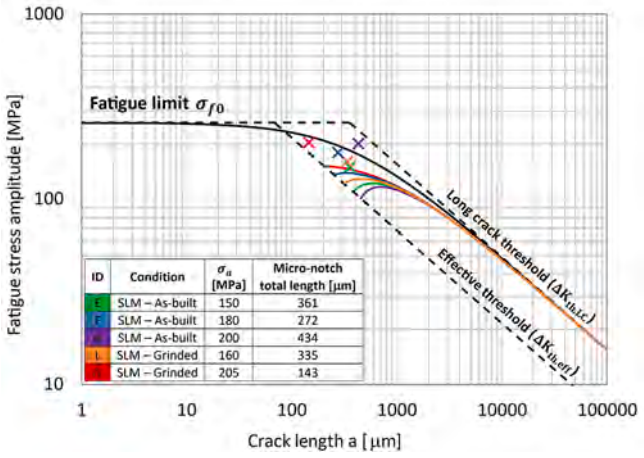

Fig. 13. Limit curves and experimental data points in the K-T diagram for a selection of the broken fatigue specimens summarized in Table 7.

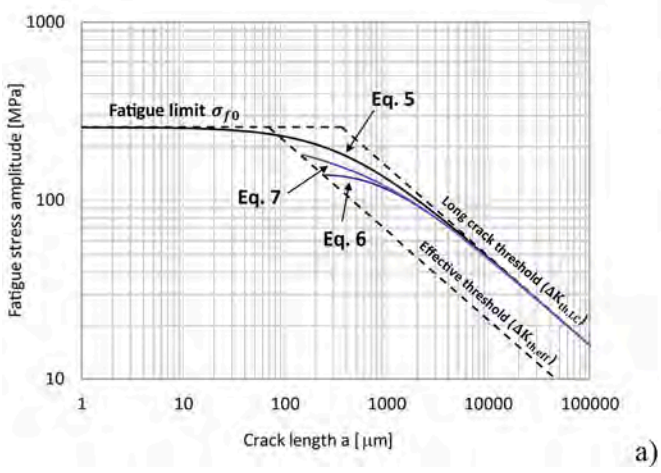

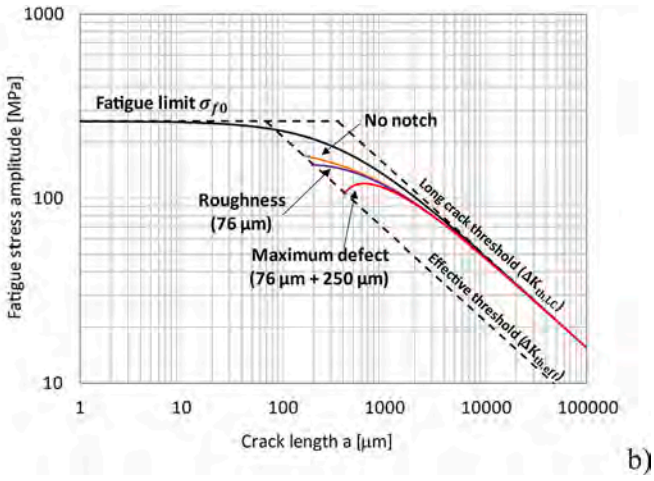

Fig. 12. a) Comparison among the limit curves according to the proposed models in the K-T diagram; b) Comparison among the limit curves varying the length of the equivalent micro-notch.

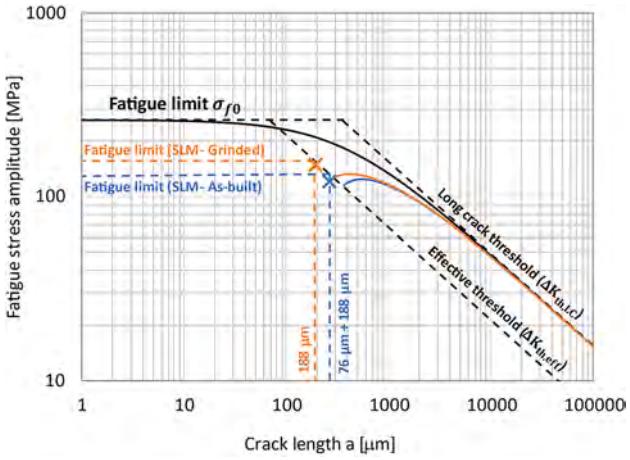

Fig. 14. Estimation of the Wöhler fatigue limits at 50 % survival probability in the as-built and grinded SLMed conditions.

Table 9
Comparison between the experimental and the predicted Wöhler fatigue limits at 50 % survival probability.

	Total micro-notch length [µm]	σ_f (experimental) [MPa]	σ_f (predicted) [MPa]	% Error
As-built	188 + 76	120	131	9.2
Grinded	188	150	157	4.7

obtained with Equation (7) varying the initial micro-notch length. In particular, the ideal curve without initial micro-notch is compared to that associated with the equivalent micro-notch of the surface roughness and that related to the equivalent micro-notch of the maximum surface defect observed in the metallographic analysis.

As reported before, the fracture surfaces of some broken fatigue specimens were analysed by SEM. Crack nucleations occurred at the surface because of the surface roughness or the combined effect of roughness and near-surface defects. Failure was investigated and confirmed in each condition using the K-T diagram. A selection of the broken fatigue specimens summarized in Table 7 is reported on the K-T diagram shown in Fig. 13. As previously described, the limit curve for non-propagating cracks varies in each condition depending on the initial total equivalent micro-notch length. Considering the El-Haddad expression for the limit curve defined by Equation (5), only the failure of sample G would have been supported by this model since all the others fall in the safe zone. This observation confirms the non-conservativeness of the El-Haddad model.

According to the results shown in Fig. 7.f, the maximum defect size present in 50 % of the fatigue specimens is equal to 188 µm. This value is adopted to estimate the Wöhler fatigue limit at 50 % survival probability in both the grinded and as-built conditions. Particularly, regarding the as-built condition, the total defect size was obtained adding the equivalent micro-notch associated to the surface roughness, i. e. 76 µm. In Fig. 14, the fatigue limits were determined as the stresses associated to the defect sizes of 188 µm and 264 µm (188 µm + 76 µm), respectively. The comparison between the experimental and the predicted values is reported in Table 9.

4. Conclusions

This research work underlines the importance of surface roughness and defects in determining fatigue limits. However, thanks to the high ductility of 316L stainless steel, good defect tolerance is present. For this reason, reduction of the fatigue limit in the as-built condition compared to the contour-free one is not severe and the surface coefficient, b_2, is equal to 0.8. The analysis of fatigue limits and failures from the threshold perspective based on fracture mechanics principles confirmed the experimental results and the non-conservativeness of the El-Haddad model. Then, this work outlines the possibility of predicting Wöhler fatigue limits considering in the Kitagawa-Takahashi diagram the equivalent total micro-notch length at 50 % probability determined by metallographic analysis.

Funding Source

This research did not receive any specific grant from funding agencies in the public, commercial, or not-for-profit sectors.

Declaration of Competing Interest

The authors declare that they have no known competing financial interests or personal relationships that could have appeared to influence the work reported in this paper.

Data availability

The data that has been used is confidential.

References

[1] Sanaei N, Fatemi A. Defects in additive manufactured metals and their effect on fatigue performance: A state-of-the-art review. Prog Mater Sci 2021;117. https://doi.org/10.1016/j.pmatsci.2020.100724.
[2] Zhang M, Sun CN, Zhang X, Wei J, Hardacre D, Li H. Predictive models for fatigue property of laser powder bed fusion stainless steel 316L. Mater Des 2018;145:42–54. https://doi.org/10.1016/j.matdes.2018.02.054.
[3] Liverani E, Toschi S, Ceschini L, Fortunato A. Effect of selective laser melting (SLM) process parameters on microstructure and mechanical properties of 316L austenitic stainless steel. J Mater Process Technol 2017;249:255–63. https://doi.org/10.1016/j.jmatprotec.2017.05.042.
[4] Shamsujjoha Md, Agnew SR, Fitz-Gerald JM, Moore WR, Newman TA. High Strength and Ductility of Additively Manufactured 316L Stainless Steel Explained. Metall Mater Trans A 2018;49:3011–27. https://doi.org/10.1007/s11661-018-4607-2.
[5] Tolosa I, Garciandía F, Zubiri F, Zapirain F, Esnaola A. Study of mechanical properties of AISI 316 stainless steel processed by "selective laser melting", following different manufacturing strategies. Int J Adv Manuf Technol 2010;51:639–47. https://doi.org/10.1007/s00170-010-2631-5.
[6] Lewandowski JJ, Seifi M. Metal Additive Manufacturing: A Review of Mechanical Properties. Annu Rev Mater Res 2016;46:151–86. https://doi.org/10.1146/annurev-matsci-070115-032024.
[7] Shrestha R, Simsiriwong J, Shamsaei N. Fatigue behavior of additive manufactured 316L stainless steel parts: Effects of layer orientation and surface roughness. Addit Manuf 2019;28:23–38. https://doi.org/10.1016/j.addma.2019.04.011.
[8] Suryawanshi J, Prashanth KG, Ramamurty U. Mechanical behavior of selective laser melted 316L stainless steel. Mater Sci Eng A 2017;696:113–21. https://doi.org/10.1016/j.msea.2017.04.058.
[9] Elangeswaran C, Cutolo A, Muralidharan GK, de Formanoir C, Berto F, Vanmeensel K, et al. Effect of post-treatments on the fatigue behaviour of 316L stainless steel manufactured by laser powder bed fusion. Int J Fatigue 2019;123:31–9. https://doi.org/10.1016/j.ijfatigue.2019.01.013.
[10] Mower TM, Long MJ. Mechanical behavior of additive manufactured, powder-bed laser-fused materials. Mater Sci Eng A 2016;651:198–213. https://doi.org/10.1016/j.msea.2015.10.068.
[11] Stern F, Kleinhorst J, Tenkamp J, Walther F. Investigation of the anisotropic cyclic damage behavior of selective laser melted AISI 316L stainless steel. Fatigue Fract Eng Mater Struct 2019;42:2422–30. https://doi.org/10.1111/ffe.13029.
[12] Andreau O, Pessard E, Koutiri I, Penot JD, Dupuy C, Saintier N, et al. A competition between the contour and hatching zones on the high cycle fatigue behaviour of a 316L stainless steel: Analyzed using X-ray computed tomography. Mater Sci Eng A 2019;757:146–59. https://doi.org/10.1016/j.msea.2019.04.101.
[13] Zhang M, Sun CN, Zhang X, Goh PC, Wei J, Hardacre D, et al. Fatigue and fracture behaviour of laser powder bed fusion stainless steel 316L: Influence of processing parameters. Mater Sci Eng A 2017;703:251–61. https://doi.org/10.1016/j.msea.2017.07.071.
[14] Riemer A, Leuders S, Thöne M, Richard HA, Tröster T, Niendorf T. On the fatigue crack growth behavior in 316L stainless steel manufactured by selective laser melting. Eng Fract Mech 2014;120:15–25. https://doi.org/10.1016/j.engfracmech.2014.03.008.
[15] Casati R, Lemke J, Vedani M. Microstructure and Fracture Behavior of 316L Austenitic Stainless Steel Produced by Selective Laser Melting. J Mater Sci Technol 2016;32:738–44. https://doi.org/10.1016/j.jmst.2016.06.016.

[16] Cao Y, Moumni Z, Zhu J, Zhang Y, You Y, Zhang W. Comparative investigation of the fatigue limit of additive-manufactured and rolled 316 steel based on self-heating approach. Eng Fract Mech 2020;223. https://doi.org/10.1016/j.engfracmech.2019.106746.

[17] Gerosa R, Rivolta B, Tavasci A, Silva G, Bergmark A. Crack initiation and propagation in Chromium pre-alloyed PM-steel under cyclic loading. Eng Fract Mech 2008;75:750–9. https://doi.org/10.1016/j.engfracmech.2007.01.009.

[18] Rivolta B, Gerosa R, Silva G, Tavasci A, Engstrom U. Wear performances of surface hardened PM steel from pre-alloyed powder. Wear 2012;289:160–7. https://doi.org/10.1016/j.wear.2012.04.001.

[19] Spierings AB, Starr TL, Wegener K. Fatigue performance of additive manufactured metallic parts. Rapid Prototyp J 2013;19:88–94. https://doi.org/10.1108/13552541311302932.

[20] Mohammad KA, Ali A, Sahari BB, Abdullah S. Fatigue behavior of austenitic type 316L stainless steel. IOP Conf Ser Mater Sci Eng 2012. https://doi.org/10.1088/1757-899X/36/1/012012.

[21] Strizak JP, Tian H, Liaw PK, Mansur LK. Fatigue properties of type 316LN stainless steel in air and mercury, in. J Nucl Mater 2005:134–44. https://doi.org/10.1016/j.jnucmat.2005.03.019.

[22] Solberg K, Guan S, Razavi SMJ, Welo T, Chan KC, Berto F. Fatigue of additively manufactured 316L stainless steel: The influence of porosity and surface roughness. Fatigue Fract Eng Mater Struct 2019;42:2043–52. https://doi.org/10.1111/ffe.13077.

[23] H. Masuo, Y. Tanaka, S. Morokoshi, H. Yagura, T. Uchida, Y. Yamamoto, Y. Murakami, Effects of Defects, Surface Roughness and HIP on Fatigue Strength of Ti-6Al-4V manufactured by Additive Manufacturing, in: Procedia Structural Integrity, Elsevier B.V., 2017: pp. 19–26. https://doi.org/10.1016/j.prostr.2017.11.055.

[24] Donzella G, Gerosa R, Petrogalli C, Rivolta B, Silva G, Beretta M. Evaluation of the residual stresses induced by shot peening on some sintered steels, in. Procedia Eng, Elsevier Ltd 2011:3399–404. https://doi.org/10.1016/j.proeng.2011.04.560.

[25] Bocchini GF, Rivolta B, Gerosa R. Universal hardness test to characterize PM steels. Int J Powder Metall 2008;44:77–84.

[26] Firrao D, Gerosa R, Ghidini A, Matteis P, Mortarino G, Pinasco MR, et al. Relation between fatigue crack initiation and propagation, toughness and microstructure in large steel blooms for automotive plastic molds. Int J Fatigue 2007;29:1880–4. https://doi.org/10.1016/j.ijfatigue.2007.01.015.

[27] S. Baragetti, R. Gerosa, G. Silva, B. Rivolta, Effect of shot peening on the fatigue behavior of some sintered steels, in: Key Eng Mater, Trans Tech Publications Ltd, 2012: pp. 511–514. https://doi.org/10.4028/www.scientific.net/KEM.488-489.511.

[28] Bocchini GF, Rivolta B, Silva G, Poggio E, Pinasco MR, Ienco MG. Microstructural and mechanical characterisation of some sinter hardening alloys and comparisons with heat treated PM steels. Powder Metall 2004;47:343–51. https://doi.org/10.1179/003258904X14464.

[29] Bocchini GF, Pinasco MR, Rivolta B, Silva G, Stagno E. Sinter hardening of low-alloy steels: influence of part geometry and physical properties of the material. Int J Mater Prod Technol 2007;28:312. https://doi.org/10.1504/IJMPT.2007.013083.

[30] Bocchini GF, Ienco MG, Pinasco MR, Stagno E, Baggioli A, Gerosa R, et al. Nominally Equivalent Powders for P/M Steels: Analysis of Response to Sintering and Differences at Various C Content. Mater Sci Forum 2007;534–536:701–4. https://doi.org/10.4028/www.scientific.net/MSF.534-536.701.

[31] Bocchini G, Ienco M, Pellati G, Pinasco M, Baggioli A, Gerosa R, et al. Comparison of the characteristics of sintered steels from nominally equivalent powders sintered at 1125°C. Metallurgia Italiana 2007;99:21–6.

[32] Rivolta B, Pinasco M, Bocchini G. Fractographic investigation on some sinter-hardened steels. Metallurgia Italiana 2002;94:29–34.

[33] Bocchini G, Piccardo P, Pinasco M, Rivolta B, Silva G, Stagno E. Response to carbonitriding heat treatment of a PM steel, from a diffusion bonded power, sintered in different conditions. Metallurgia Italiana 2001;93:39–48.

[34] Bocchini G, Ienco M, Pinasco M, Stagno E, Rivolta B, Silva G. Physical, microstructural and mechanical characterization of a steel obtained from powder diffusion bonded in various sintering conditions. Metallurgia Italiana 1999;91:61–8.

[35] Bocchini G, Baggioll A, Gerosa R, Rivolta B, Silva G. Cooling rates of P/M steels. Int J Powder Metall 2004;40:57–65.

[36] Yasa E, Kruth JP. Microstructural investigation of selective laser melting 316L stainless steel parts exposed to laser re-melting. in: Procedia Eng, Elsevier Ltd; 2011. p. 389–95.

[37] Alrbaey K, Wimpenny DI, Al-Barzinjy AA, Moroz A. Electropolishing of Re-melted SLM Stainless Steel 316L Parts Using Deep Eutectic Solvents: 3 × 3 Full Factorial Design. J Mater Eng Perform 2016;25:2836–46. https://doi.org/10.1007/s11665-016-2140-2.

[38] Scipioni Bertoli U, MacDonald BE, Schoenung JM. Stability of cellular microstructure in laser powder bed fusion of 316L stainless steel. Mater Sci Eng A 2019;739:109–17. https://doi.org/10.1016/j.msea.2018.10.051.

[39] Bartolomeu F, Buciumeanu M, Pinto E, Alves N, Carvalho O, Silva FS, et al. 316L stainless steel mechanical and tribological behavior—A comparison between selective laser melting, hot pressing and conventional casting. Addit Manuf 2017;16:81–9. https://doi.org/10.1016/j.addma.2017.05.007.

[40] Avanzini A. Fatigue Behavior of Additively Manufactured Stainless Steel 316L. Materials 2023;16. https://doi.org/10.3390/ma16010065.

[41] Uhlmann E, Fleck C, Gerlitzky G, Faltin F. Dynamical Fatigue Behavior of Additive Manufactured Products for a Fundamental Life cycle Approach. in: Procedia CIRP, Elsevier B.V; 2017. p. 588–93.

[42] Shrestha R, Simsiriwong J, Shamsaei N. Fatigue behavior of additive manufactured 316L stainless steel under axial versus rotating-bending loading: Synergistic effects of stress gradient, surface roughness, and volumetric defects. Int J Fatigue 2021;144. https://doi.org/10.1016/j.ijfatigue.2020.106063.

[43] R. Shrestha, J. Simsiriwong, N. Shamsaei, Comparison of Rotating-Bending and Axial Fatigue Behaviors of LB-PBF 316L Stainless Steel, in: 30th Annual International Solid Freeform Fabrication Symposium – An Additive Manufacturing Conference, 2019: pp. 515–521.

[44] Kumar P, Jayaraj R, Suryawanshi J, Satwik UR, McKinnell J, Ramamurty U. Fatigue strength of additively manufactured 316L austenitic stainless steel. Acta Mater 2020;199:225–39. https://doi.org/10.1016/j.actamat.2020.08.033.

[45] Puchi-Cabrera ES, Matínez F, Herrera I, Berríos JA, Dixit S, Bhat D. On the fatigue behavior of an AISI 316L stainless steel coated with a PVD TiN deposit. Surf Coat Technol 2004;182:276–86. https://doi.org/10.1016/j.surfcoat.2003.07.003.

[46] S. Lampman, Fatigue and Fracture Properties of Stainless Steels, in: Fatigue and Fracture, ASM International, 1996: pp. 712–732. https://doi.org/10.31399/asm.hb.v19.a0002403.

[47] Murakami Y. Metal Fatigue. Elsevier 2002. https://doi.org/10.1016/B978-0-08-044064-4.X5000-2.

[48] BSI Standards Publication, BS ISO 1143:2021: Metallic materials - Rotating bar bending fatigue testing, (2021).

[49] BSI Standards Publication, BS ISO 12107:2012: Metallic materials — Fatigue testing — Statistical planning and analysis of data, BSI. (2012).

[50] BSI Standards, ISO 21920–2:2022: Geometrical product specifications (GPS) — Surface texture: Profile - Part 2: Terms, definitions and surface texture parameters, (2022).

[51] BSI Standards Publication, BS EN ISO 6892–1:2019: Metallic materials - Tensile testing, (2020).

[52] BSI Standards, ISO 6507-1:2018: Metallic materials – Vickers hardness test, (2018).

[53] Sausto F, Carrion PE, Shamsaei N, Beretta S. Fatigue failure mechanisms for AlSi10Mg manufactured by L-PBF under axial and torsional loads: The role of defects and residual stresses. Int J Fatigue 2022;162. https://doi.org/10.1016/j.ijfatigue.2022.106903.

[54] Beretta S, Patriarca L, Gargourimotlagh M, Hardaker A, Brackett D, Salimian M, et al. A benchmark activity on the fatigue life assessment of AlSi10Mg components manufactured by L-PBF. Mater Des 2022;218. https://doi.org/10.1016/j.matdes.2022.110713.

[55] Beretta S, Gargourimotlagh M, Foletti S, du Plessis A, Riccio M. Fatigue strength assessment of "as built" AlSi10Mg manufactured by SLM with different build orientations. Int J Fatigue 2020;139. https://doi.org/10.1016/j.ijfatigue.2020.105737.

[56] ASTM International, E407-07: Standard Practice for Microetching Metals and Alloys, (2015).

[57] el Haddad MH, Smith KN, Topper TH. Fatigue Crack Propagation of Short Cracks. J Eng Mater Technol 1979;101:42–6. https://doi.org/10.1115/1.3443647.

[58] H. Kitagawa, Applicability of fracture mechanics to very small cracks or the cracks in the early stage, in: 2nd ICM, Cleveland, 1976: pp. 627–631.

[59] Pippan R, Berger M, Stliwe HP. The Influence of Crack Length on Fatigue Crack Growth in Deep Sharp Notches. Metall Trans A 1987;18:429–35.

[60] Tanaka K, Akiniwa Y. Resistance-curve method for predicting propagation threshold of short fatigue cracks at notches. Eng Fract Mech 1988;30:863–76. https://doi.org/10.1016/0013-7944(88)90146-4.

[61] Chapetti M. Fatigue propagation threshold of short cracks under constant amplitude loading. Int J Fatigue 2003;25:1319–26. https://doi.org/10.1016/S0142-1123(03)00065-3.

[62] McEvily AJ, Minakawa K. On crack closure and the notch size effect in fatigue. Eng Fract Mech 1987;28:519–27. https://doi.org/10.1016/0013-7944(87)90049-X.

[63] Zerbst U, Madia M. Fracture mechanics based assessment of the fatigue strength: approach for the determination of the initial crack size. Fatigue Fract Eng Mater Struct 2015;38:1066–75. https://doi.org/10.1111/ffe.12288.

[64] Li B, Rosa LG. Prediction models of intrinsic fatigue threshold in metal alloys examined by experimental data. Int J Fatigue 2016;82:616–23. https://doi.org/10.1016/j.ijfatigue.2015.09.018.

[65] Hertzberg RW. On the calculation of closure-free fatigue crack propagation data in monolithic metal alloys. Mater Sci Eng A 1995;190:25–32. https://doi.org/10.1016/0921-5093(94)09610-9.

[66] Pippan R, Riemelmoser FO. Modeling of Fatigue Crack Growth: Dislocation Models. In: Comprehensive Structural Integrity. Elsevier; 2003. p. 191–207. https://doi.org/10.1016/B0-08-043749-4/04035-0.

[67] Maierhofer J, Gänser H-P, Pippan R. Modified Kitagawa-Takahashi diagram accounting for finite notch depths. Int J Fatigue 2015;70:503–9. https://doi.org/10.1016/j.ijfatigue.2014.07.007.

[68] P. Andreini, Manuale dell'ingegnere meccanico, 3rd ed., Ulrico Hoepli Editore S.p. A., Milan, 2021.

[70] Wood P, Libura T, Kowalewski ZL, Williams G, Serjouei A. Influences of Horizontal and Vertical Build Orientations and Post-Fabrication Processes on the Fatigue Behavior of Stainless Steel 316L Produced by Selective Laser Melting. Materials 2019;12:4203. https://doi.org/10.3390/ma12244203.

[71] Bergant M, Werner T, Madia M, Yawny A, Zerbst U. Short crack propagation analysis and fatigue strength assessment of additively manufactured materials: An application to AISI 316L. Int J Fatigue 2021;151. https://doi.org/10.1016/j.ijfatigue.2021.106396.

[72] Hasegawa K, Strnadel B, Usami S, Lacroix V. Fatigue Crack Growth Thresholds at Negative Stress Ratio for Ferritic Steels in ASME Code Section XI, Journal of Pressure Vessel Technology. Transactions of the ASME 2019;141. https://doi.org/10.1115/1.4043081.

[73] Samuel KG, Sasikala G, Ray SK. On R ratio dependence of threshold stress intensity factor range for fatigue crack growth in type 316(N) stainless steel weld. Mater Sci Technol 2011;27:371–6. https://doi.org/10.1179/026708310X12699498463048.
[74] Pourheidar A, Patriarca L, Beretta S, Regazzi D. Investigation of fatigue crack growth in full-scale railway axles subjected to service load spectra: Experiments and predictive models. Metals (Basel) 2021;11. https://doi.org/10.3390/met11091427.
[75] A.J. McEvily, Fatigue Crack Thresholds, in: Fatigue and Fracture, ASM International, 2018: pp. 134–152. https://doi.org/10.31399/asm.hb.v19.a0002357.
[76] Zerbst U, Bruno G, Buffière JY, Wegener T, Niendorf T, Wu T, et al. Damage tolerant design of additively manufactured metallic components subjected to cyclic loading: State of the art and challenges. Prog Mater Sci 2021;121. https://doi.org/10.1016/j.pmatsci.2021.100786.
[77] Hasegawa K, Dvořák D, Mareš V, Strnadel B, Usami S. Suitability of fatigue crack growth thresholds at negative stress ratios for ferritic steels and aluminum alloys in flaw evaluation procedures. Eng Fract Mech 2021;248. https://doi.org/10.1016/j.engfracmech.2021.107670.